Kinetic analysis of the plasma sheath around an electron-emitting object with elliptic cross section

Luca Chiabó,* Sadaf Shahsavani, and Gonzalo Sánchez-Arriaga
Bioengineering and Aerospace Engineering Department, Universidad Carlos III de Madrid, Leganés, Madrid 28911, Spain

(Received 2 August 2021; accepted 21 October 2021; published 12 November 2021)

The structure of the sheath and the current exchange of two-dimensional electron-emitting objects with elliptic cross section immersed at rest in Maxwellian plasmas are investigated with an energy-conserving stationary Vlasov-Poisson solver free of statistical noise. The parameter domains for current collection within the orbital-motion-limited (OML) regime and current emission in space-charge-limited (SCL) conditions were studied by varying the characteristic dimension of the ellipse, its eccentricity, and the emission level. The analysis reveals the correlations between the onset of the non-OML and SCL regimes and the local curvature of the ellipse. As compared to nonemitting ellipses, electron emission broadens the parameter domain for OML current collection for ions and reduces considerably the current drop for non-OML conditions. Under identical plasma environments, elliptic bodies are more prone to operate under non-OML and SCL conditions than cylinders. Their emitted current in SCL conditions can be computed accurately from well-known results for cylinders if appropriate dimensionless variables and an equivalent radius are used. The role of the eccentricity, which acts as an integrability-breaking parameter, on the filamentation of the distribution function of the attracted species is studied.

DOI: 10.1103/PhysRevE.104.055204

I. INTRODUCTION

Sheath structures arising from the self-organization of a plasma surrounding an object are ubiquitous in plasma physics [1]. Langmuir probes (LPs) and emissive probes (EPs) [2–8], charging of grains in complex plasmas [9–12], spacecraft charging [13–16], and current collection and emission by electrodynamic tethers (EDTs) [17–20] are some interesting examples. Kinetic descriptions, involving complex analytical analysis and significant computational resources in numerical simulations, are typically required to correctly capture essential features of the sheaths. An example is the appearance of an electrostatic potential well close to electron-emitting objects, resulting in space-charge-limited (SCL) emission. Important theoretical efforts were made in the past to study configurations with simple geometries (e.g., planes, cylinders, and spheres). Their symmetries yield conserved quantities, like momentum or angular momentum of charged particles, that can be exploited to reduce the dimensions of the problem and obtain relatively simple models [21–24]. Nonetheless, for many interesting scenarios such conservation laws do not hold. Relevant examples include objects with less regular geometries, such as nonspherical dust grains [25] and EDTs with tapelike cross sections [26,27], plasma probes with finite lengths [28], plasma-sheath lenses [29–31], and objects with simple shapes but immersed in flowing plasmas [32–34].

Several works have dealt with geometries that do not yield conserved quantities for particle orbits. Laframboise and Parker showed that orbital-motion-limited (OML) current holds for *sufficiently convex* objects [35]. Assessment of OML validity for a thin, taped cross section in the limit of high bias was carried out by Sanmartín and Estes in [22], who generalized their results to prisms of infinite length and arbitrary cross section in [36]. Though useful, such analytical and semianalytical models are subject to the fulfillment of several assumptions (high bias, infinite length, etc). Their relaxation requires numerical simulations, thus leading to the development of different codes for investigating plasma sheaths and current collection and emission. For instance, a Vlasov-Poisson solver based on a backward Liouville method [37] was used to investigate Langmuir probes with tapelike cross section in a wide range of biases [38]. The sheath around elongated dust grains in flowing plasmas was studied with a particle-in-cell (PIC) code in [39]. More recently, results on the charging of nonspherical dust grain were obtained with a treecode [40] and benchmarked against recent analytical models [41] that extend the work of [35] to spheroids of higher aspect ratios.

This work presents quantitative results of the steady-state sheath around an infinitely long electron-emitting object with an elliptic cross section immersed at rest in Maxwellian plasmas. This is a particularly interesting case due to its connection with several applications in plasma physics and aerospace engineering. For instance, the proposed scenario may be a convenient approximation of nonspherical dust grains. Additionally, when the eccentricity e_p is close to 1, the results of this work can be applied to tapelike EDTs, which are deemed to outperform cylindrical ones [26,27,42]. In particular, the so-called low-work-function tether (LWT) [18,20] has a cathodic segment whose physical configuration is similar to the one discussed in this work. Besides these applications, the sheath around an electron-emitting ellipse is a relevant theoretical problem. Unlike cylinders, ellipses have no

*Corresponding author: lchiabo@pa.uc3m.es

axial symmetry, and the angular momentum is not conserved along particle trajectories. This feature opens the possibility of having chaotic dynamics for the trapped particles and filamentation of the distribution function, which can affect the convergence of stationary Vlasov-Poisson solvers [43]. Therefore the eccentricity (e_p) acts as an integrability-breaking parameter, i.e., the orbits are regular for $e_p = 0$, and chaos can appear for $e_p \neq 0$. Finally, the analysis fills the theoretical gap between the orbital motion theory (OMT) for probes with cylindrical [21,24] and tapelike cross sections [22,38] and studies the transition from regular to filamented distribution functions. The boundaries that separate OML/non-OML and SCL/non-SCL operation conditions in parameter space are investigated too.

Such novel analysis has been eased by the use of a recently developed code based on a backward Liouville method to solve the Vlasov-Poisson system self-consistently [43]. Unlike particle-in-cell codes and stationary Vlasov-Poisson solvers used in the past to study nonintegrable configurations [28,38], the code is free of statistical noise and conserves the energy along particle trajectories. Consequently, the filamentation of the distribution functions and the transition between different current collection and emission regimes can be studied accurately. In Sec. II the main equations of the model and the structure of the numerical algorithm are described. Section III investigates the macroscopic quantities of the plasma sheath for elliptic configurations. In Sec. IV, the operational regimes of (electron-emitting) elliptic bodies are investigated, with particular focus on the impact of the eccentricity, the semiminor axis-to-Debye length ratio, and the emission level. Comparisons with available results regarding cylinders and tapes without emission are provided. Section V discusses interesting kinetic features induced by elliptic geometries. The main conclusions and application of the results are presented in Sec. VI.

II. A KINETIC MODEL FOR ELECTRON-EMITTING AND ELLIPTIC OBJECTS

The model considers a two-dimensional ellipse of eccentricity e_p and semiminor axis B_p immersed at rest in a collisionless, unmagnetized, Maxwellian plasma made of electrons and ions with unperturbed density N_0 and temperatures T_{e0} and T_{i0}, respectively. The object is biased at Φ_P with respect to the unperturbed plasma, and it emits electrons following a half-Maxwellian distribution function with density N_{em0} and temperature T_{em0}. For convenience, we introduce the following normalized quantities:

$$\boldsymbol{r} \equiv \frac{\boldsymbol{R}}{\lambda_{De}}, \quad \boldsymbol{v} \equiv \frac{\boldsymbol{V}}{v_{th\alpha}}, \quad n_{e,i} \equiv \frac{N_{e,i}}{N_0}, \quad n_{em} \equiv \frac{N_{em}}{N_{em0}}, \tag{1}$$

$$f_\alpha(\boldsymbol{r}, \boldsymbol{v}) \equiv \frac{2k_B T_\alpha F_\alpha}{m_\alpha N_{\alpha 0}}, \quad \phi(\boldsymbol{r}) \equiv \frac{e\Phi}{k_B T_e}, \tag{2}$$

with $\boldsymbol{R}$ and $\boldsymbol{V}$ the position and velocity vectors, F_α the distribution function, Φ the electrostatic potential, $\lambda_{De} \equiv \sqrt{\epsilon_0 k_B T_e / e^2 N_0}$ the electron Debye length, $v_{th\alpha} \equiv \sqrt{2k_B T_\alpha / m_\alpha}$ the thermal velocities, k_B the Boltzmann constant, ϵ_0 the vacuum permittivity, e the elementary charge, and m_α the mass of the species. In Eq. (1) and hereafter, the subscript α identifies plasma electrons ($\alpha = e$), plasma ions ($\alpha = i$), and emitted electrons ($\alpha = em$). In stationary conditions, the dimensionless distribution functions and electrostatic potential obey the stationary Vlasov-Poisson system,

$$\boldsymbol{v} \cdot \nabla f_\alpha - \frac{e_\alpha}{2\delta_\alpha} \nabla\phi \cdot \nabla_v f_\alpha = 0, \tag{3a}$$

$$\Delta\phi = -\rho \equiv n_e + \beta n_{em} - e_i n_i. \tag{3b}$$

Its solutions depend on the dimensionless parameters

$$\delta_\alpha \equiv \frac{T_{\alpha 0}}{T_{e0}}, \quad e_\alpha \equiv \frac{q_\alpha}{e}, \quad \beta \equiv \frac{N_{em0}}{N_0}, \tag{4}$$

$$\phi_P \equiv \frac{e\Phi_P}{k_B T_{e0}}, \quad b_p = \frac{B_p}{\lambda_{De}}, \quad e_p, \tag{5}$$

where q_α is the charge of the species. The dimensionless densities at the right-hand side of Eq. (3b) are obtained by

$$n_\alpha(\boldsymbol{r}) = \int_{-\infty}^{+\infty} f_\alpha(\boldsymbol{r}, \boldsymbol{v}) d\boldsymbol{v}. \tag{6}$$

Regarding the boundary conditions, at the contour of the object

$$\Gamma = \left\{(x, y) | \left(1 - e_p^2\right)x^2 + y^2 = b_p^2\right\}, \tag{7}$$

we have

$$\phi(\Gamma) = \phi_P \tag{8}$$

$$f_{em}(\Gamma, \boldsymbol{v} \cdot \boldsymbol{u}_n > 0) = f_{HM} \equiv \frac{2}{\pi} \exp\{-(\boldsymbol{v} \cdot \boldsymbol{v})\}, \tag{9}$$

with $\boldsymbol{u}_n$ the outward unit vector normal to Γ. Far away from the object, the conditions are

$$\phi(r \to \infty) \to 0, \tag{10}$$

$$f_{e,i}(r \to \infty, \boldsymbol{v}) \to f_M \equiv \frac{1}{\pi} \exp\{-(\boldsymbol{v} \cdot \boldsymbol{v})\}, \tag{11}$$

with $r = \sqrt{x^2 + y^2}$.

For $e_p \neq 0$, the solutions of system Eqs. (3a) and (3b) are found with the algorithm of Ref. [43] referred to as *FDM-CN*, which is the one with the best performances and accuracy. Its computational domain is defined by the inner boundary Γ and an outer boundary $\Gamma_{\max}$ identifying an ellipse confocal to Γ and normalized semiminor axis $b_{\max}$ large enough to recover quasineutrality. Such a domain is discretized on a uniform mesh in (curvilinear) elliptical coordinates. The unknowns of the algorithm are the N values of the space-charge vector $\boldsymbol{\rho} \in \mathcal{R}^N$ at the nodes of the mesh, which is found by implementing a Newton-Raphson method that solves

$$\boldsymbol{G}(\boldsymbol{\rho}) \equiv \boldsymbol{\rho} - \mathcal{V}[\mathcal{P}(\boldsymbol{\rho})] = 0. \tag{12}$$

The iterative procedure stops when $|| \boldsymbol{G} ||_2 < Tol$, with Tol a given tolerance. The operator $\mathcal{P}$ is a Poisson solver based on a finite-difference method (FDM) that receives the space charge and finds the electrostatic potential. Since the spatial domain is truncated, the boundary condition $\phi \approx 1/r$ was set at $\Gamma_{\max}$ [38,43].

Operator $\mathcal{V}$ is a Vlasov solver based on a backward Liouville scheme [37]. Receiving the electrostatic potential $\phi(x, y)$

as input, it computes the distribution function f_α by the backward integration of the characteristics of the Vlasov equation:

$$\frac{d\boldsymbol{r}}{d\tau} = \boldsymbol{v}, \tag{13a}$$

$$\frac{d\boldsymbol{v}}{d\tau} = -\frac{e_\alpha}{2\delta_\alpha}\nabla\phi, \tag{13b}$$

with τ parametrizing the integral curves. Being the distribution function conserved along the characteristics (collisionless plasma), the value of $f_\alpha(\boldsymbol{x}_{s0})$ is found by integrating Eqs. (13a) and (13b) numerically with initial conditions $\boldsymbol{x}_{s0} = (\boldsymbol{r}_0, \boldsymbol{v}_0)$ until the trajectory ends up at a boundary of the computational domain where the distribution function is known. We assign $f_{e,i}(\boldsymbol{x}_{s0}) = f_M$ and $f_{em}(\boldsymbol{x}_{s0}) = 0$ [$f_{e,i}(\boldsymbol{x}_{s0}) = 0$ and $f_{em}(\boldsymbol{x}_{s0}) = f_{HM}$] if the orbit hits $\Gamma_{\max}$ (Γ). For brevity, we will refer to these orbits as $\Gamma_{\max}$-*originated* and Γ-*originated*. If the orbit performs N_{tr} loops around the ellipse, then the code sets $f_\alpha(\boldsymbol{x}_{s0}) = 0$ with $\alpha = e, i, em$, and the particle is classified as *trapped*.

Since the energy is conserved along the orbits, we substitute (v_x, v_y) by (ϵ_α, ζ), with

$$\epsilon_\alpha \equiv v_x^2 + v_y^2 + \frac{e_\alpha}{\delta_\alpha}[\phi(x,y) - a_\alpha\phi_p], \tag{14}$$

$$\zeta \equiv \tan^{-1}\left(\frac{\boldsymbol{v}\cdot\boldsymbol{t}}{\boldsymbol{v}\cdot\boldsymbol{n}}\right), \tag{15}$$

the (dimensionless) energy of the charged particle and an angle in velocity space, and $\boldsymbol{t}$ and $\boldsymbol{n}$ the tangential and normal (outward) unit vectors to the ellipse confocal with Γ passing through (x, y), $a_{e,i} = 0$, and $a_{em} = 1$. For each point (x, y), the Vlasov solver defines a grid of $N_\epsilon \times N_\zeta$ nodes discretizing the domain $(\epsilon_\alpha, \zeta) \in [\epsilon_\alpha^{\min}\ \epsilon_\alpha^{\max}] \times [0\ 2\pi]$, with $\epsilon_\alpha^{\min} \equiv max\{0, [\phi(x,y) - a_p\phi_p](e_\alpha/\delta_\alpha)\}$ and $\epsilon_\alpha^{\max}$ a high enough numerical parameter. Each point $\boldsymbol{z}_0 = [x^i, y^j, \epsilon_\alpha^k, \zeta^l]$ provides the initial conditions for the numerical integration of Eqs. (13a) and (13b), which is carried out with a hybrid, implicit Crank-Nicolson (CN) scheme that exactly conserves the energy originally proposed for the particle-in-cell codes of [44–46]. Its implementation in the framework of stationary conditions with nonperiodic boundary conditions is described in [43]. Unlike PIC algorithms, simulations based on a backward Liouville scheme are free of statistical noise and suitable to investigate fine kinetic features (e.g., filamentation) of the plasma sheath [37]. More details about the implementation of solvers $\mathcal{P}$ and $\mathcal{V}$ are in Ref. [43] and references therein.

For $e_p = 0$ (cylinders), the system of Eqs. (3a) and (3b) requires solving Eq. (12) as well. Due to the azimuthal symmetry, both the Vlasov and Poisson solvers simplify notably. Reference [24] contains the details of the numerical code, which has recently been used to create a broad database of current-voltage characteristics for emissive cylinders [47].

Once the space-charge vector satisfying Eq. (12) is found, the distribution functions f_α and any other macroscopic quantities of interest can be computed. For instance, the particle densities are given by Eq. (6), and the electric current collected or emitted by the object per unit length is

$$I_\alpha = eN_0\sqrt{\frac{k_B T_e}{2\pi m_e}} \times p \times j_\alpha, \tag{16}$$

where p is the perimeter of the ellipse and

$$j_\alpha \equiv e_\alpha\sqrt{\frac{\delta_\alpha}{\mu_\alpha}}\frac{\sqrt{\pi}}{p_p}\int_0^p j_s(s)ds \tag{17}$$

with

$$j_s(s) \equiv \int_{-\infty}^{+\infty}\int_{-\infty}^{+\infty}(\boldsymbol{v}\cdot\boldsymbol{u}_n)f_\alpha(\Gamma, v_x, v_y)dv_x dv_y, \tag{18}$$

$\mu_\alpha \equiv m_\alpha/m_e$, $j_s(s)$ the local normalized current per unit area, and s the arc length along Γ [see Eq. (A3)] measured from the point $(x, y) = (a_p, 0) \equiv (b_p/\sqrt{1-e_p^2}, 0)$, with a_p the (normalized) semimajor axis of the ellipse. Typical numerical values used in this work are

$$N \sim 10^3, \quad N_\epsilon = 150, \quad N_\eta = 360, \quad N_{tr} = 2 \tag{19}$$

$$b_{\max} \sim 10^1, \quad \epsilon_\alpha^{\max} = \epsilon_\alpha^{\min} + 6, \quad Tol = 5\times10^{-3}. \tag{20}$$

As shown below, we explored a broad space of physical parameters by varying geometrical, background plasma, and electron emission properties. Nonetheless, the parameter domain was mainly targeted to ionospheric plasmas, where the hypotheses of the orbital motion theory (like the collisionless character of the plasma) hold reasonably. As a reference, we consider here typical values in the ionosphere for the plasma density ($N_0 = 10^{11}$ m^{-3}) and temperatures ($T_e \approx T_i \approx 0.15$ eV) that give a Debye length of $\lambda_D \approx 1$ cm and $\delta_i = 1$. For a typical tapelike tether of width 3 cm at temperature $T_t = 550$ K, one obtains $a_p = 1.5$, which corresponds to $b_p \approx 1$ for $e_p = 0.75$, and $\delta_{em} = 0.32$. Moderate values of ϕ_p and a broad range of β were considered in order to explore the transition from SCL to non-SCL conditions. These parameters, which cover space plasmas and tether applications, are close to those used in Ref. [24] for cylinders.

III. SHEATH STRUCTURE

This section characterizes the plasma sheath around ellipses of different properties. The effect of the eccentricity is studied by considering the parameters

$$0 \leqslant e_p \leqslant 0.99, \quad \phi_p = -4.0, \quad b_p = 1.0,$$
$$\delta_i = 1.0, \quad \delta_{em} = 0, \quad \beta = 0. \tag{21}$$

Panels (a) and (b) in Fig. 1 show the charge density [see Eq. (3b)] at the horizontal and vertical axes of the computational domain, respectively. Taking the round case ($e_p = 0$) as baseline [dark grey lines with circles], we observe that the charge grows up to a maximum and then decreases monotonically with the distance. Due to the azimuthal symmetry, the two lines are identical. For $e_p > 0$, axial symmetry does not hold and the profiles differ in the neighborhood of Γ. Such an effect is enhanced for higher values of e_p, which yield more extended sheaths as well. Since both symmetry and quasineutrality are recovered as $r \to \infty$, larger computational boxes (i.e., bigger $b_{\max}$) are used for higher values of e_p.

The eccentricity affects the position and intensity of the maximum of ρ too. The former approaches the object as e_p increases. Such effect is stronger at the semiminor axis where, for $e_p \to 1$, the maximum is practically at the object and ρ

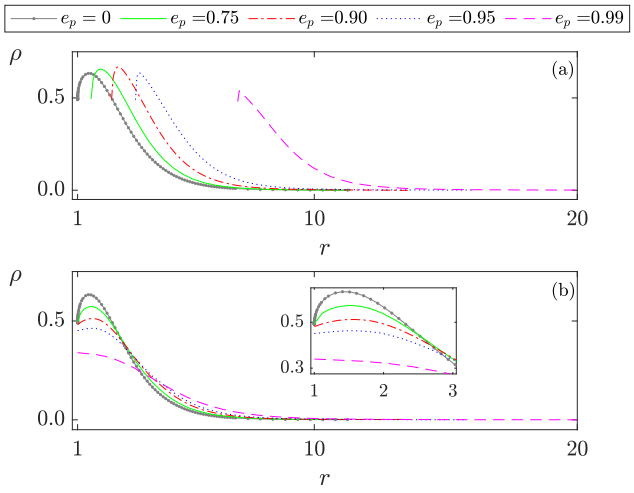

FIG. 1. Space charge at the $y = 0$ [panel (a)] and $x = 0$ [panel (b)] axes for several eccentricities.

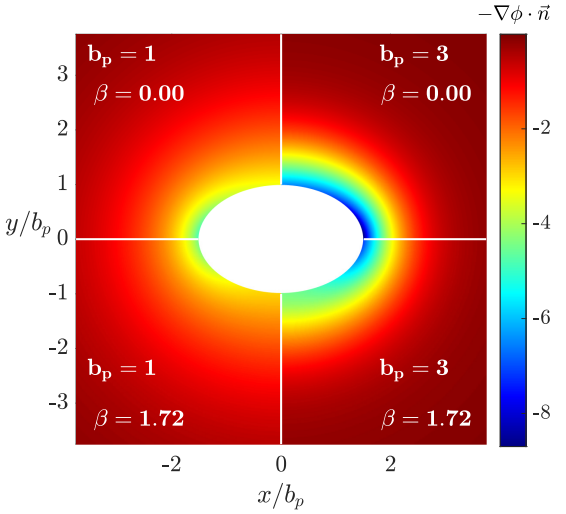

FIG. 3. Normal component of the electric field for $e_p = 0.75$, $\delta_i = 1$, $\delta_p = -5$.

decays almost monotonically. Regarding its value, at $y = 0$ [panel (a)] the maximum is barely constant up to $e_p = 0.95$, while it decreases as $e_p \to 1$ following a growth in the number of Γ-originated ion orbits. More details and quantitative results supporting this statement are given in Sec. V. At $x = 0$ [panel (b)], the maximum of the density decreases monotonically with e_p.

The roles of the characteristic size of the object to the Debye length (b_p) and the emission level (β) were analyzed by running four simulations with the parameters

$$e_p = 0.75, \quad \phi_p = -5.0, \quad 1 \leqslant b_p \leqslant 3,$$
$$\delta_i = 1.0, \quad \delta_{em} = 0.32, \quad \beta = \{0,\ 1.72\}. \qquad (22)$$

The four quadrants of Fig. 2 show the density of the attracted ions in the neighborhood of Γ. Since $e_p = 0.75$, the ion density is not axisymmetric. A comparison of the two top and bottom panels reveals that the electron emission enhances the dependence of the density with the azimuthal angle. This is

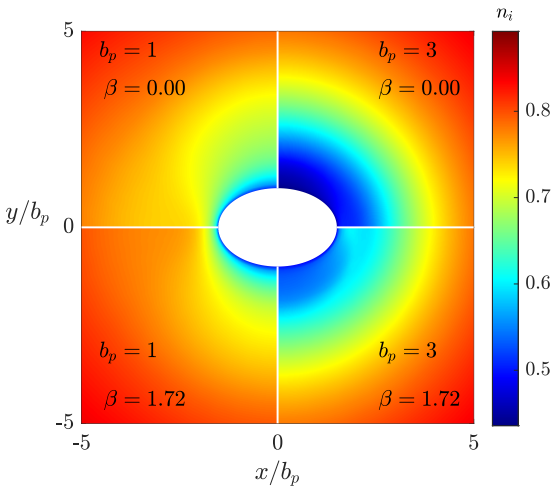

FIG. 2. Detail of the density of attracted ions inside the sheath for $e_p = 0.75$, $\delta_i = 1$, $\phi_p = -5$.

particularly evident close to the x axis. An inspection of the left and right panels unveils that increasing b_p has the opposite effect. For larger b_p, the local curvature [see Eq. (A4)] of the ellipse decreases and the sheath is less sensitive to the particular shape of Γ. When moving away from Γ, the ion density grows much slower for $b_p = 3$ than for $b_p = 1$. In particular, the top-right panel ($\beta = 0$) exhibits a broad region with ion density below 0.6 surrounding the ellipse. Consequently, we conclude that the size of the sheath increases with b_p, a result consistent with previous works on infinite cylinders [17,21,38].

Understanding this effect requires analyzing the electric field component normal to the ellipse confocal to Γ at each point. As shown in Fig. 3, an inward (negative) electric force exists for the attracted ions. Stronger electric fields and larger objects yield more Γ-originated orbits that result in a lower density of the attracted species. A comparison of the left and right panels in Fig. 3 shows that the normal component of the electric field is stronger for larger b_p. Electron emission (bottom panels) mitigates the electric field, yielding a higher ion density close to Γ.

IV. OPERATIONAL REGIMES

This section discusses different operational regimes for electron collection and emission when varying (i) the eccentricity e_p, (ii) the characteristic dimension b_p, and (iii) the emission level β.

A. Transition between OML and non-OML operational regimes

The OML regime occurs when no barriers of effective potential that could prevent some particles from reaching Γ occur [35]. Current collection is maximum for OML conditions, and important and very general results hold. For instance, for a two-dimensional object of arbitrary shape and negatively polarized with respect to the ambient plasma

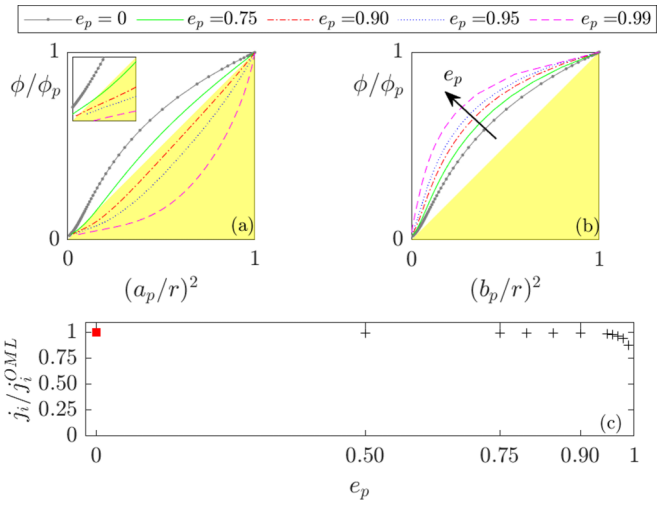

FIG. 4. Electrostatic potential at the $y = 0$ [panel (a)] and $x = 0$ [panel (b)] axes for several eccentricities. Collected current-to-OML current ratio vs the eccentricity [panel (c)].

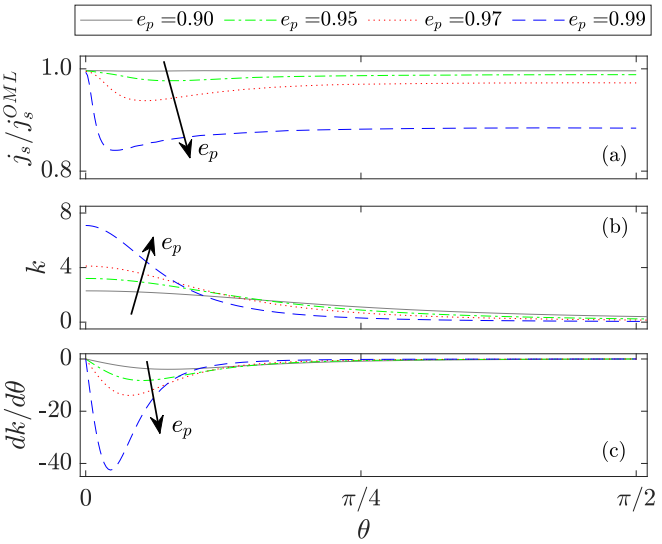

FIG. 5. Ratio $j_s(\theta)/j_s^{\mathrm{OML}}$ (a), curvature k (b), and $dk/d\theta$ (c) vs the azimuthal angle θ for several eccentricities.

operating in OML conditions, the ions (attracted species) satisfy

$$n_i^{\mathrm{OML}}(\Gamma) = \frac{1}{2}, \tag{23}$$

$$j_i^{\mathrm{OML}}(\Gamma) = \sqrt{\frac{\delta_i}{\mu_i}}\left[2\sqrt{-\frac{\chi_\alpha}{\pi}} + \exp(\chi_i)\cdot erfc(\sqrt{\chi_i})\right], \tag{24}$$

with $\chi_i \equiv -\phi_p/\delta_i$ [35]. Therefore the determination of the parameter domain yielding OML conditions is a very relevant theoretical problem. Important efforts were made in the past to address it. Theoretical results were obtained for nonemitting cylinders, thin tapes, and infinite prisms with convex and concave cross sections in the high-bias limit [22,36], and spheroids in the Laplace limit [35]. For electron-emitting cylinders, the OML parameter domain has been found recently [47]. The VP solver allows one to revisit previous results, typically based on asymptotic analysis and sensible approximations, and to explore deeper the role of the electron emission.

1. Slenderness of the object

To understand the role of the slenderness of the object, panels (a) and (b) in Fig. 4 show the electrostatic potential at $x = 0$ and $y = 0$ for several eccentricities and the parameters of Eq. (21). Since for $e_p = 0$ the OML condition reads $R_p^2\Phi_p \leqslant R^2\Phi(R)$, i.e., the OML current collection [see Eq. (24)] holds if the electrostatic potential profiles does not cross the diagonal [22], we display the bias versus a_p^2/r^2 and b_p^2/r^2, respectively. Results show that increasing e_p pushes the electrostatic potential profile into the non-OML region for cylinders [see panel (a) and its inset]. However, such a region is not the non-OML domain for ellipses. As shown in panel (c), displaying the ratio j_i/j_i^{OML} versus e_p, ellipses with eccentricities up to $e_p = 0.90$ collect the OML current (at least up to the precision of our numerical calculations), although their profiles penetrate the filled region in the top panels. The OML/non-OML transition lies between $0.90 \leqslant e_p \leqslant 0.95$, an outcome aligned with the analysis in the Laplace limit of Ref. [35], which predicted such transition to happen for oblate spheroids of aspect ratio 2.537 ($e_p \approx 0.92$). As e_p further increases, the object resembles a tape and the current ratio reaches $j_i/j_i^{\mathrm{OML}} \approx 0.88$. Such a value is lower than the ≈1% drop predicted for a thin tape at very high bias [22]. Thus high-bias conditions mitigate the effect of the shape of Γ on current collection. For a given b_p, the reduction in j_i is largely counterbalanced by the increase in the perimeter with e_p [see Eq. (16)]. For instance, one has $p\,|_{e_p=0.99} = 4.9 \times p\,|_{e_p=0}$ and $p\,|_{e_p=0.99} = 2.71 \times p\,|_{e_p=0.9}$.

Panel (a) in Fig. 5, which shows the ratio $j_s(\theta)/j_s^{\mathrm{OML}}$ versus the azimuthal angle θ [see Eqs. (18), (A1) and (A2)], provides useful information about the spatial distribution of the current collection along Γ. Due to the symmetry, only a quarter of the ellipse is considered. Up to around $e_p = 0.90$ (black solid line), ions are captured uniformly along the contour because OML conditions hold. For $e_p > 0.9$, the current is OML at $\theta = 0$ [$(x, y) = (a_p, 0)$]. The current ratio then decreases to a minimum and grows back monotonically up to a value lower than 1 and is barely constant for $\theta > \pi/8$. Points collecting OML and non-OML current coexist along Γ. Being the density of the repelled species practically zero, such a result is consistent with the values of the charge density at the ellipse shown in panels (a) and (b) of Fig. 1. The charge density is equal to 0.5 at the horizontal axis and below 0.5 at the vertical axis [see Eq. (24)].

The behavior of $j_s(\theta)/j_s^{\mathrm{OML}}$ versus θ is strongly correlated with the local curvature of the ellipse [see Eq. (A4)] displayed in panel (b). Around $\theta = \pi/2$, the curvature is low, and the ellipse is not *convex enough* to reach OML current collection. However, this does not imply $(x, y) = (0, b_p)$ being the point of minimum current collection. As shown in panel (c), such a minimum occurs where the curvature k undergoes the highest change in magnitude and moves closer to $\theta = 0$ as e_p grows. Such a result highlights the impact of the geometry of the plasma-surface interface on the current collection,

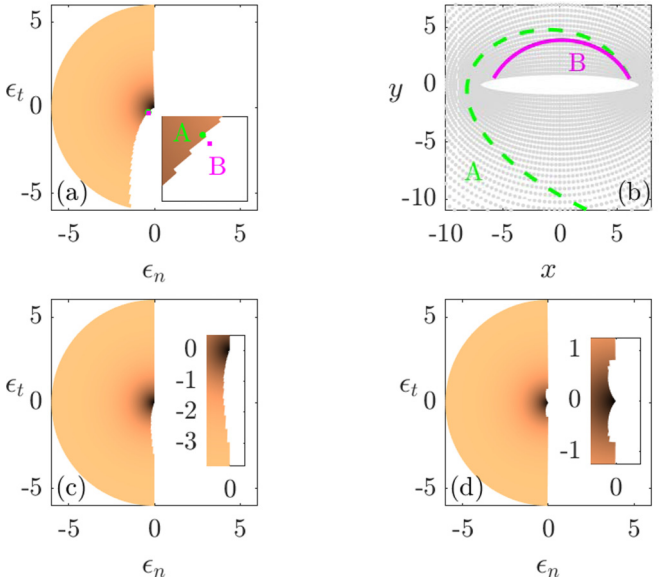

FIG. 6. Ion distribution functions for $e_p = 0.99$ (a) and 0.95 (c) evaluated at Γ and the value of θ where a minimum is reached for panel (a) in Fig. 4. Panel (b) shows two orbits for the initial conditions labeled with A and B in panel (a). Panel (d) displays the ion distribution function at Γ for a cylinder ($e_p = 0$) of perimeter equal to the ellipse of panel (a).

which is relevant in the plasma-sheath lens-related applications [29–31].

Understanding the $j_s(\theta)/j_s^{\mathrm{OML}}$ minimum requires a kinetic analysis of the distribution function in velocity space or, for convenience, in the $\epsilon_n - \epsilon_t$ plane [38,48], with

$$\epsilon_n \equiv \epsilon_\alpha \cdot \cos\zeta\,, \tag{25}$$

$$\epsilon_t \equiv \epsilon_\alpha \cdot \sin\zeta\,. \tag{26}$$

Panels (a) and (c) in Fig. 6 display the ion distribution function for $e_p = 0.99$ and $e_p = 0.95$ at Γ and the value of θ yielding the minimum for $j_s(\theta)/j_s^{\mathrm{OML}}$. For $\epsilon_n > 0$, both diagrams are empty because the probe does not emit ions. Interestingly, as e_p increases, an unpopulated region with $\epsilon_t < 0$ and $\epsilon_n < 0$ develops and grows, explaining the lower value of the $j_s(\theta)/j_s^{\mathrm{OML}}$ minimum for $e_p = 0.99$ than for $e_p = 0.95$. Owing to the elliptic geometry, trajectories with $\pi \leqslant \zeta \leqslant 3\pi/2$ travel across a vast area surrounding Γ, where they are deflected towards it. For a given energy, a value of ζ close enough to $3\pi/2$ [see panel (a)] yields Γ-originated orbits [see orbit B in panel (b)]. The higher the eccentricity, the larger the number of such orbits, while panel (c) displays how the span of ζ angles yielding B-like trajectories decreases with the energy.

A comparison between the current collected by an ellipse of $e_p = 0.99$ and a cylinder of the same perimeter closes this section. The latter, which operates in non-OML conditions as well, presents two unpopulated regions symmetric with respect the ϵ_t axis [see panel (d) of Fig. 6]. However, their impact on the current collection is smaller as one obtains $j_i\,|_{e_p=0} = 1.08\, j_i\,|_{e_p=0.99}$.

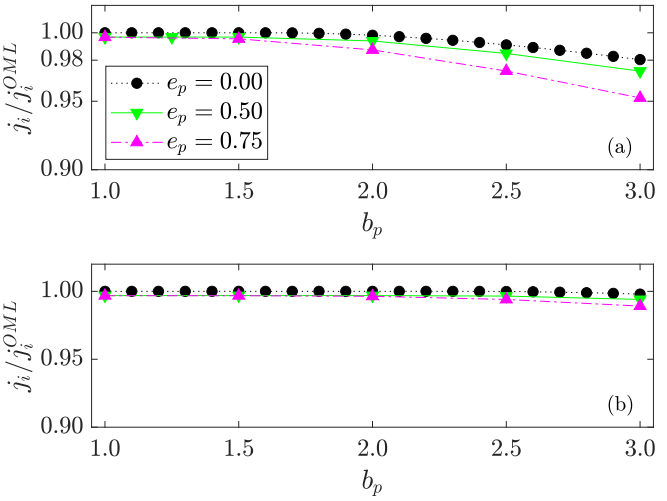

FIG. 7. Collected-to-OML current vs b_p for several eccentricities. Panels (a) and (b) correspond to $\beta = \delta_{em} = 0$ and $\beta = 1.72$ and $\delta_{em} = 0.32$, respectively.

2. *Characteristic dimension*

Convex enough objects collects OML current if their characteristic dimension is small enough as compared with the Debye length [35]. Quantitative results are here presented for ellipses by finding the solutions of the VP system for $\delta_i = 1.0$, $\phi_p = -5$, $\beta = 0$, and

$$e_p = \{0,\ 0.5,\ 0.75\} \quad 1 \leqslant b_p \leqslant 3.$$

As expected, the ratio $j_i/j_i^{\mathrm{OML}} = 1$ in panel (a) of Fig. 7 when b_p is small for the three eccentricities. However, as b_p increases, the attracted ions must cover longer paths in presence of a stronger electric field near Γ (see Fig. 3) without hitting it in order to contribute to the current collection [see panel (b) of Fig. 6].

For a cylinder ($e_p = 0$), the transition happens for radius around $1.5\lambda_{DE}$ [47], but even larger radii do not produce a significant reduction of the ratio. The current ratio drops weakly with b_p for low-bias conditions ($\phi_p = -5$ in our case) as well as for high-bias ones [49].

Non-OML current collection occurs for lower values of b_p for ellipses with higher eccentricities, though the current decreases smoothly. For instance, doubling and tripling b_p for $e_p = 0.75$ yield a drop of about 2% and 5%, respectively. Such results resemble previous analyses for tapes [38] and two-dimensional prisms of any shape in the limit of high bias [36]. Therefore a good agreement exists between the outcomes of the analysis and those obtained in previous works, as well as between the collected currents predicted by the two independent Vlasov-Poisson solvers for cylinders and ellipses shown in Fig. 7 (computed with two independent solvers). Overall, the results show that the shape of Γ (eccentricity) affects the current collection more significantly than its size.

3. *Electron emission*

The role of the electron emission on the OML/non-OML transition was investigated by solving the VP system with the same parameters of the previous section but setting $\beta = 1.72$

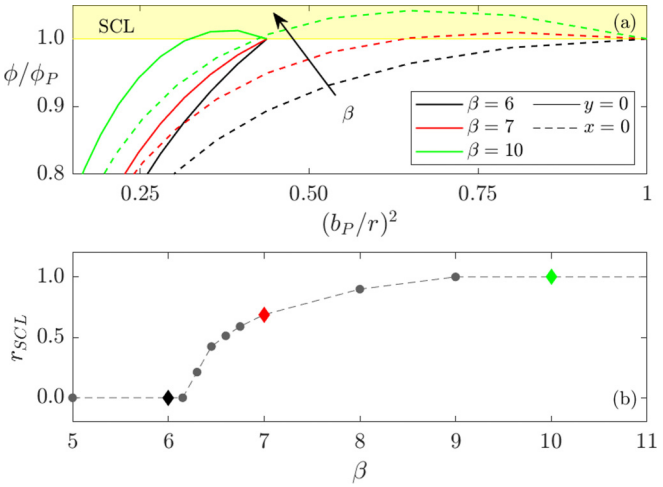

FIG. 8. Panel (a): normalized electrostatic potential profile vs $(b_p/r)^2$ for several emission levels at $x = 0$ (dashed) and $y = 0$ (solid). Panel (b): fraction of the perimeter under SCL conditions vs emission level β.

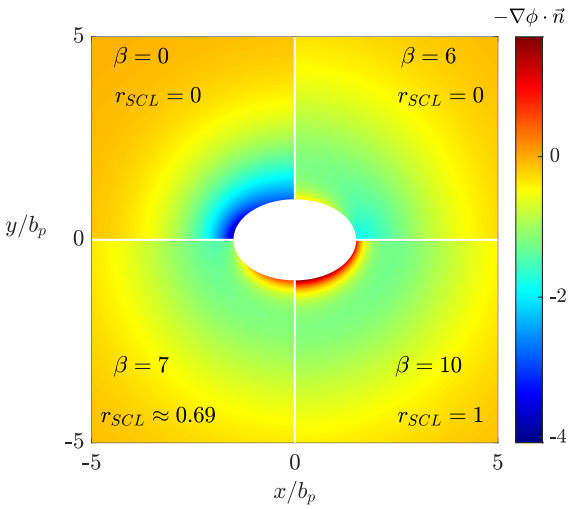

FIG. 9. Normal component of the electric field for $e_p = 0.75$, $\delta_i = 1$, $\phi_p = -4$, $\delta_{em} = 0.32$.

and $\delta_{em} = 0.32$. As shown in panel (b) of Fig. 7, the emission of electrons delays the transition into the non-OML regime to higher b_p. Such a result, which was previously found for cylinders [24,47], is a consequence of the reduction of the electric field in the proximity of Γ due to the higher density of electrons (see Fig. 3), yielding in turn a reduction of Γ-originated ions. Even when b_p is such that non-OML conditions hold, the ratio is $j_i/j_i^{\rm OML} \approx 1$ for the three eccentricities considered. Therefore, in the presence of electron emission, the OML current law holds for a broader range of physical parameters (eccentricities and sizes). This is an important result for applications involving modeling of object-plasma current exchange such as probes, dusty plasmas, and space tethers.

B. Transition between non-SCL and SCL operational regimes

For fixed values of δ_i, e_p, b_p, and $\phi_p < 0$, a potential dip can develop close to the plasma-body interface as the emission level (β and δ_{em}) increases. Under such SCL conditions, the electric field reverses and some of the emitted electrons are reflected back to Γ. This interesting physical scenario is studied by finding solutions for

$$e_p = 0.75, \quad \phi_p = -4.0, \quad b_p = 1.0,$$
$$\delta_i = 1.0, \quad \delta_{em} = 0.32, \quad 0 \leqslant \beta \leqslant 30. \tag{27}$$

The non-SCL/SCL transition for electron-emitting ellipses is characterized by analyzing the potential profile and the fraction of the perimeter of the ellipse under SCL conditions to the total perimeter ($r_{\rm SCL} = p_{\rm SCL}/p$) (Fig. 8), the normal component of the electric field (Fig. 9), and the distribution function of emitted electrons at particular points of Γ (Fig. 10). For convenience, the potential profile will be plotted again versus $(b_p/r)^2$. In that diagram, a normalized potential profile above the horizontal line $\phi/\phi_p = 1$ [panel (a) in Fig. 8] corresponds to a potential well in the ϕ/ϕ_p versus r plane (not shown).

For $\beta < 6.2$, electron emission is non-SCL. As shown in panel (a) of Fig. 8 and the top panels of Fig. 9, there is no potential dip (monotonic potential profile) and the electric field points inward everywhere. The distribution functions of the emitted electrons are filled with outgoing (i.e., $\epsilon_n \geqslant 0$) particles only, as all the emitted electrons are driven away by the electric field [panels (a) and (d) in Fig. 10]. However, as shown in panel (a) of Fig. 8, the electric field at Γ for $x = 0$, where the curvature is minimum, is almost zero.

Within the range $6.2 < \beta < 9$, non-SCL and SCL conditions coexist. For $\beta = 7.00$ (solid and dashed red lines in Fig. 8), the electrostatic potential at $x = 0$ enters the SCL regime (yellow area), while it is still monotonic for $y = 0$. The bottom left panel of Fig. 9 shows the reversion of the electric field in the proximity of $(x, y) = (0, b_p)$. At that point, emitted electrons appear for $\epsilon_n < 0$ (incoming particles), whereas the same region is left unpopulated at $(x, y) = (a_p, 0)$ [panels (b) and (e) in Fig. 10, respectively]. For $\beta > 9$, the whole

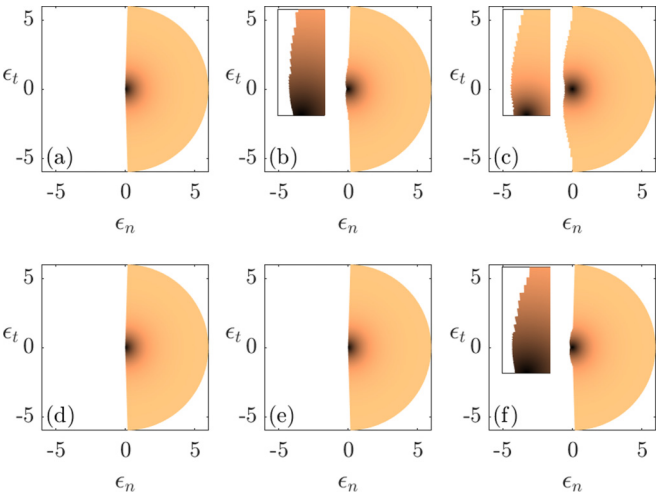

FIG. 10. Normalized distribution functions for emitted electrons (f_{em}) at $(x, y) = (0, b_p)$ [panels (a), (b) and (c)] and $(x, y) = (a_p = 0)$ [panels (d), (e), and (f)] for $\beta = 6$ [panels (a) and (d)], $\beta = 7$ [panels (b) and (e)], and $\beta = 10$ [panels (c) and (f)], respectively.

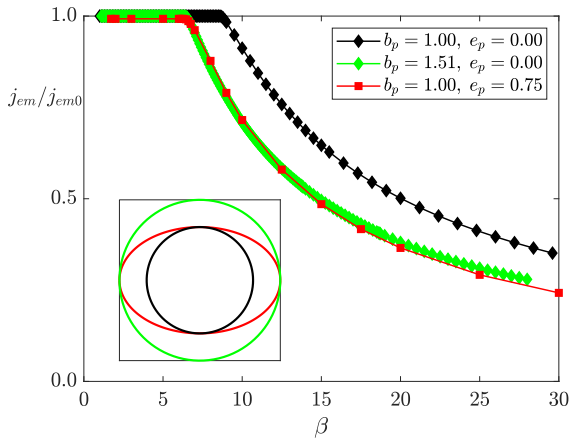

FIG. 11. Emitted-to-half-Maxwellian current vs β.

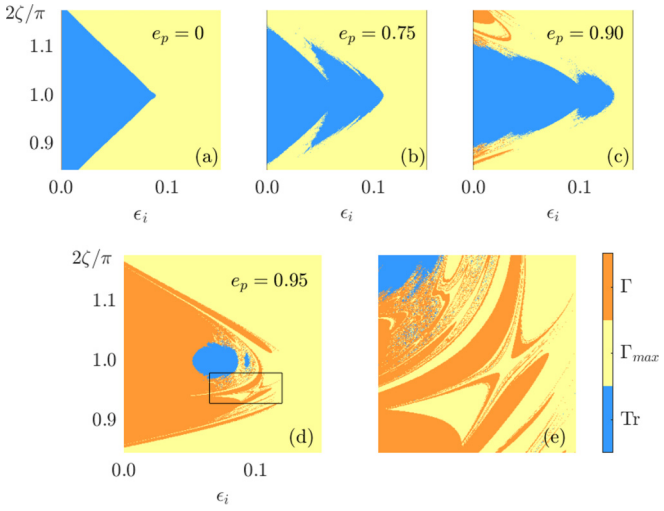

FIG. 12. Domains in the $\epsilon_i - \zeta$ plane of the ion distribution function at $(x, y) \approx (3.4, 0)$ for $e_p = 0$ (a), $e_p = 0.75$ (b), $e_p = 0.9$ (c), and $e_p = 0.95$ (d). Panel (e) shows a detail of the region marked with a rectangle in panel (d). Orange, yellow, and blue colors identify Γ-originated, $\Gamma_{\max}$-originated, and trapped orbits, respectively.

perimeter is SCL ($r_{\rm SCL} = 1$) and the electrostatic potential is nonmonotonic at both $x = 0$ and $y = 0$ (Fig. 8). The potential dip covers a wider region of the sheath as well (bottom right panel of Fig. 9). Accordingly, the spans of energies filled up by incoming particles in panels (c) and (f) of Fig. 10 are bigger.

The impact of the SCL regime on the emitted current is shown in Fig. 11, which presents the variation of j_{em}/j_{em0} for a wide range of emission levels for the three bodies shown in the inset. Here

$$j_{em0} = -2\beta\sqrt{\delta_{em}} \tag{28}$$

is the current emitted by a half-Maxwellian, i.e., the current emitted under non-SCL conditions.

The red line with squares corresponds to an ellipse with $e_p = 0.75$, while the black (green) line with diamond (stars) was obtained for a cylinder with radius equal to the semiminor (-major) axis of the ellipse. At low β, $j_{em}/j_{em0} = 1$ for the three objects. As β increases, each body enters the SCL regime and the emitted current decreases. Such a transition occurs at $\beta \approx 6.5$ for both the ellipse and the cylinder of highest radius. The two curves follow a similar trend, despite the transition occurring gradually along Γ for $e_p = 0.75$. Unlike the impact of b_p on $j_i/j_i^{\rm OML}$, which is weak, the ratio j_{em}/j_{em0} is much more sensitive to β for the three cases, and drops in the current emission of about 50% are achieved for $\beta \sim 15$. The numerical results show that the current emitted by ellipses at moderate bias can be approximated with good accuracy by that emitted by cylinders of radius equal to the semimajor axis, if appropriate dimensionless variables are used. A broad, recently built database of solutions for electron-emitting cylinders [47] can thus be used for ellipses.

V. FILAMENTATION

The characteristic Eqs. (13a) and (13b) are a four-dimensional Hamiltonian system. Since the Hamiltonian is τ independent, the energy ϵ_α in Eq. (14) is conserved along the orbits. When $e_p = 0$, the electrostatic potential profile is axisymmetric and the angular momentum is also conserved. Provided there are two invariants, the phase space has effective dimension $4 - 2 = 2$, the system is *integrable*, and its solutions regular. Two consequences are (i) a numerical integration of the orbits is not necessary to compute the distribution function [24], and (ii) the boundaries in velocity space separating empty and filled regions of the distribution function are smooth curves, as shown in panel (a) of Fig. 12. For $e_p = 0$, and the parameters values

$$\phi_p = -4.0, \quad b_p = 1.0, \quad \delta_i = 1.0, \quad \delta_{em} = 0, \quad \beta = 0, \tag{29}$$

the boundary between regions of $\Gamma_{\max}$-originated ($f_i = f_M$) and trapped ($f_i = 0$) orbits is smooth. The diagram was obtained by using a high-resolution grid ($N_\epsilon \times N_\zeta = 300 \times 300$) in velocity space and the self-consistent numerical potential profile.

For $e_p \neq 0$, the angular momentum is not conserved and the effective dimension of Eqs. (13a) and (13b) is $4 - 1 = 3$. Consequently, chaotic orbits can appear and the distribution function can be very complex in velocity space [43]. As shown in panels (b), (c), and (d) in Fig. 12, obtained for $N_{tr} = 100$ and the parameters of Eq. (29), the structure of f_i becomes more complex as e_p increases. For $e_p = 0.75$, the boundaries separating trapped from nontrapped particles are jagged, and for $e_p = 0.9$, a population of Γ-originating ions with $f_i = 0$ appears due to the larger perimeter of the ellipse (see Sec. IV A). The different types of orbits are deeply mixed in velocity space and the distribution function is filamented as a consequence of the nonintegrable character of the system for $e_p \neq 0$. For $e_p = 0.95$ [panel (d)] and the detail in panel (e), such mixing is even deeper. The boundaries have a complex geometry, and the distribution function is highly discontinuous, jumping between 0 (trapped, Γ-originated orbits) and finite positive values ($\Gamma_{\max}$-originated orbits). A proper selection of the grid resolution in velocity space and an appropriate choice of N_{tr} help filtering such discontinuities [43], which can affect the convergence of the solution.

VI. CONCLUSIONS

A stationary Vlasov-Poisson solver was used to investigate the sheath around electron-emitting bodies with an elliptic cross section Γ. Although common hypotheses in orbital motion theory (OMT) analysis were taken, like the absence of trapped particles, magnetic field, and collisions, the solver is free of statistical noise and conserves the energy exactly. A broad range of physical parameters was explored but focused on typical conditions for dusty plasma, spacecraft charging, and space tethers orbiting in ionospheric plasmas, where OMT hypotheses hold reasonably. Quantitative results on the current collection and emission and their domains of operation were obtained as a function of the geometry of the object, the plasma properties, and the emission level.

It was shown that the characteristic dimension-to-Debye length ratio (b_p) shields the dependence of the macroscopic quantities with the azimuthal angle, while both the emission level (β) and the eccentricity (e_p) of the ellipse enhance such features. Eccentricity was also shown to have a major effect on current collection. For a given b_p, the population of Γ-originated particles, i.e., orbits that hit the object when integrated backwards in time, increases with e_p. If the slenderness is above a certain threshold, the collected current falls below the OML limit. The critical eccentricity value for OML/non-OML transition is in agreement with previous analytical works for oblate spheroids in the Laplace limit. Reasonably, the current drop given by the Vlasov-Poisson solver for moderate bias is larger than that predicted for a thin tape in the high-bias limit. In fact, a high bias may mitigate the effect of the particular shape of Γ on the collected current. As compared with cylinders, and for a given perimeter, the reduction in the collected current is more severe ($\approx$8%) for ellipses. An interesting correlation between the local curvature of Γ and the current collected was also found. Unexpectedly, not only is the minimum current collected close to the point where the derivative of the curvature with the azimuthal angle is minimum rather than at the flattest portion of the ellipse, but it also approaches the semimajor axis (the point where the curvature is maximum) of Γ as e_p increases. On the other hand, the current collection drop in non-OML conditions and its dependence with the eccentricity decreases when Γ emits electrons. Therefore, regardless of the shape of the cross section, the OML current collection law can be safely used for a broader range of parameters in applications involving electron emission, such as dusty plasmas and low-work-function tethers.

Regarding current emission, the numerical analysis showed that as β increases from zero, the point of Γ of minimum curvature is the first to be SCL. For the considered parameters, the ellipse is partially SCL when the density of the emitted electrons is between six and nine times the ambient plasma density. Interestingly, the current emitted by ellipses in SCL conditions can be modeled as that emitted by cylinders with an equivalent radius equal to the semimajor axis. Since a broad database of current-voltage characteristics for electron-emitting cylinders is currently available, this result enables its application to more complex geometries upon using adequate dimensionless variables. This is an important result because, in view of the need for explicit integration of particle orbits in the Vlasov solver, the construction of a broad database for nonintegrable configurations is beyond actual numerical capabilities. The equivalent radius found in this work allows us to estimate the emitted current of ellipses by using the already available database for cylinders.

The filamentation of the distribution function of the attracted species as the eccentricity is increased is an interesting theoretical problem in plasma physics that also generates convergence issues of stationary Vlasov-Poisson solvers. This is a physical feature that affects any two-dimensional Langmuir and emissive probes without azimuthal symmetry. An open topic, which is beyond the scope of this work, is the analysis of such filamentation under the presence of collisions. Trapped particles due to collisional and nonstationary effects, both ignored in the present work, require structural modifications of the Vlasov-Poisson solver and will be addressed in a future work.

ACKNOWLEDGMENTS

This work was suppoerted by the Europen Union's Horizon 2020 FET Open project with Grant Number 828902 (E.T.PACK project).

APPENDIX: BASIC FORMULAS FOR ELLIPSES

Let us consider the parametrization

$$x(\theta) = \frac{b_p}{\sqrt{1-e_p^2}}\cos\theta, \tag{A1}$$

$$y(\theta) = b_p \sin\theta. \tag{A2}$$

The arc length measured from the x axis is

$$s(\theta) = b_p \int_0^\theta \sqrt{\frac{\sin^2 t}{1-e_p^2} + \cos^2 t}\, dt \tag{A3}$$

and the curvature

$$\kappa(\theta) = \frac{1-e_p^2}{b_p} \frac{1}{\left[\sin^2\theta + \left(1-e_p^2\right)\cos^2\theta\right]^{3/2}}. \tag{A4}$$

[1] S. D. Baalrud, B. Scheiner, B. T. Yee, M. M. Hopkins, and E. Barnat, Interaction of biased electrodes and plasmas: Sheaths, double layers, and fireballs, Plasma Sources Sci. Technol. **29**, 053001 (2020).

[2] A. Fruchtman, D. Zoler, and G. Makrinich, Potential of an emissive cylindrical probe in plasma, Phys. Rev. E **84**, 025402(R) (2011).

[3] J. P. Sheehan, E. V. Barnat, B. R. Weatherford, I. D. Kaganovich, and N. Hershkowitz, Emissive sheath measurements in the afterglow of a radio frequency plasma, Phys. Plasmas **21**, 013510 (2014).

[4] V. A. Godyak and B. M. Alexandrovich, Comparative analyses of plasma probe diagnostics techniques, J. Appl. Phys. **118**, 233302 (2015).

[5] C. Ionita, B. S. Schneider, S. Costea, O. Vasilovici, J. Kovacic, T. Gyergyek, V. Naulin, J. J. Rasmussen, N. Vianello, M. Spolaore, R. Starz, and R. Schrittwieser, Plasma potential probes for hot plasmas, Eur. Phys. J. D **73**, 73 (2019).

[6] V. I. Demidov, M. E. Koepke, I. P. Kurlyandskaya, and M. A. Malkov, Basic factors for acquiring, correcting, and interpreting probe current-voltage characteristic in moderate-collisional plasma for determining electron energy distribution, Phys. Plasmas **27**, 020501 (2020).

[7] C.-S. Yip, C. Jin, W. Zhang, G. S. Xu, and N. Hershkowitz, Experimental investigation of sheath effects on I-V traces of strongly electron emitting probes, Plasma Sources Sci. Technol. **29**, 025025 (2020).

[8] A. Olowookere and R. Marchand, Fixed bias probe measurement of a satellite floating potential, IEEE Trans. Plasma Sci. **49**(2), 862 (2021).

[9] G. L. Delzanno, G. Lapenta, and M. Rosenberg, Attractive Potential around a Thermionically Emitting Microparticle, Phys. Rev. Lett. **92**, 035002 (2004).

[10] X.-Z. Tang and G. L. Delzanno, Orbital-motion-limited theory of dust charging and plasma response, Phys. Plasmas **21**, 123708 (2014).

[11] G. L. Delzanno and X.-Z. Tang, Charging and Heat Collection by a Positively Charged Dust Grain in a Plasma, Phys. Rev. Lett. **113**, 035002 (2014).

[12] S. L. G. Hess, P. Sarrailh, J.-C. Matéo-Vélez, B. Jeanty-Ruard, F. Cipriani, J. Forest, A. Hilgers, F. Honary, B. Thiébault, S. R. Marple, and D. Rodgers, New SPIS capabilities to simulate dust electrostatic charging, transport, and contamination of lunar probes, IEEE Trans. Plasma Sci. **43**, 2799 (2015).

[13] S. Robertson, Sheaths in laboratory and space plasmas, Plasma Phys. Controlled Fusion **55**, 093001 (2013).

[14] B. Thiébault, B. Jeanty-Ruard, P. Souquet, J. Forest, J.-C. Matéo-Vélez, P. Sarrailh, D. Rodgers, A. Hilgers, F. Cipriani, D. Payan, and N. Balcon, SPIS 5.1: An innovative approach for spacecraft plasma modeling, IEEE Trans. Plasma Sci. **43**, 2782 (2015).

[15] F. L. Johansson, A. I. Eriksson, N. Gilet, P. Henri, G. Wattieaux, M. G. G. T. Taylor C. Imhof, and F. Cipriani, A charging model for the Rosetta spacecraft, A&A **642** A43 (2020).

[16] K. Zhang, S. Cai, C. Cai, and D. L. Cooke, A parallel particle-in-cell code for spacecraft charging problems, J. Plasma Phys. **86**, 905860308 (2020).

[17] J. R. Sanmartin, E. Choiniere, B. E. Gilchrist, J.-B. Ferry, and M. Martinez-Sanchez, Bare-tether sheath and current: Comparison of asymptotic theory and kinetic simulations in stationary plasma, IEEE Trans. Plasma Sci. **36**, 2851 (2008).

[18] J. D. Williams, J. R. Sanmartin, and L. P. Rand, Low work-function coating for an entirely propellantless bare electrodynamic tether, IEEE Trans. Plasma Sci. **40**, 1441 (2012).

[19] J. A. Janeski, W. A. Scales, and C. D. Hall, Investigation of the current collected by a positively biased satellite with application to electrodynamic tethers, J. Geophys. Res.: Space Physics **119**, 7824 (2014).

[20] G. Sanchez-Arriaga and X. Chen, Modeling and performance of electrodynamic low-work-function tethers with photoemission effects, J. Propul. Power **34**, 213 (2018).

[21] J. G. Laframboise, Theory of spherical and cylindrical Langmuir probes in a collisionless, Maxwellian plasma at rest, Ph.D. thesis, University of Toronto (Canada), 1966.

[22] J. R. Sanmartín and R. D. Estes, The orbital-motion-limited regime of cylindrical Langmuir probes, Phys. Plasmas **6**, 395 (1999).

[23] S. Takamura, N. Ohno, M. Y. Ye, and T. Kuwabara, Space-charge limited current from plasma-facing material surface, Contrib. Plasma Phys. **44**, 126 (2004).

[24] X. Chen and G. Sanchez-Arriaga, Orbital motion theory and operational regimes for cylindrical emissive probes, Phys. Plasmas **24**, 023504 (2017).

[25] P. M. Bellan, Why interstellar ice dust grains should be elongated, Astrophys. J. **905**, 96 (2020).

[26] S. B. Khan, A. Francesconi, C. Giacomuzzo, and E. C. Lorenzini, Survivability to orbital debris of tape tethers for end-of-life spacecraft de-orbiting, Aerosp. Sci. Technol. **52**, 167 (2016).

[27] A. Francesconi, C. Giacomuzzo, L. Bettiol, and E. Lorenzini, A new ballistic limit equation for thin tape tethers, Acta Astronaut. **129**, 325 (2016).

[28] S. Marholm and R. Marchand, Finite-length effects on cylindrical Langmuir probes, Phys. Rev. Research **2**, 023016 (2020).

[29] E. Stamate and H. Sugai, Modal Focusing Effect of Positive and Negative Ions by a Three-Dimensional Plasma-Sheath Lens, Phys. Rev. Lett. **94**, 125004 (2005).

[30] E. Stamate and H. Sugai, Discrete focusing effect of positive ions by a plasma-sheath lens, Phys. Rev. E **72**, 036407 (2005).

[31] E. Stamate, Discrete and modal focusing effects: Principles and applications, Plasma Phys. Controlled Fusion **54**, 124048 (2012).

[32] W. J. Miloch, S. V. Vladimirov, H. L. Pécseli, and J. Trulsen, Wake behind dust grains in flowing plasmas with a directed photon flux, Phys. Rev. E **77**, 065401(R) (2008).

[33] I. H. Hutchinson, Nonlinear collisionless plasma wakes of small particles, Phys. Plasmas **18**, 032111 (2011).

[34] G. Sánchez-Arriaga and D. Pastor-Moreno, Direct Vlasov simulations of electron-attracting cylindrical Langmuir probes in flowing plasmas, Phys. Plasmas **21**, 073504 (2014).

[35] J. G. Laframboise and L. W. Parker, Probe design for orbit-limited current collection, Phys. Fluids **16**, 629 (1973).

[36] J. R. Sanmartin and R. D. Estes, Interference of parallel cylindrical Langmuir probes, Phys. Plasmas **8**, 4234 (2001).

[37] R. Marchand, Test-particle simulation of space plasmas, Commun. Comput. Phys. **8**, 471 (2010).

[38] E. Choiniére, Theory and experimental evaluation of a consistent steady-state kinetic model for 2-d conductive structures in ionospheric plasmas with application to bare electrodynamic tethers in space, Ph.D. thesis, University of Michigan, 2004.

[39] W. J. Miloch, S. V. Vladimirov, H. L. Pécseli, and J. Trulsen, Numerical simulations of potential distribution for elongated insulating dust being charged by drifting plasmas, Phys. Rev. E **78**, 036411 (2008).

[40] J. T. Holgate and M. Coppins, Charging of nonspherical macroparticles in a plasma, Phys. Rev. E **93**, 033208 (2016).

[41] D. M. Thomas and J. T. Holgate, A treecode to simulate dust–plasma interactions, Plasma Phys. Controlled Fusion **59**, 025002 (2016)

[42] J. R. Sanmartn, A. Snchez-Torres, S. B. Khan, G. Snchez-Arriaga, and M. Charro, Optimum sizing of bare-tape tethers

for de-orbiting satellites at end of mission, Adv. Space Res. **56**, 1485 (2015).

[43] L. Chiabó and G. Sánchez-Arriaga, Limitations of stationary Vlasov-Poisson solvers in probe theory, J. Comput. Phys. **438**, 110366 (2021).

[44] L. Chacón, G. Chen, and D. C. Barnes, A charge- and energy-conserving implicit, electrostatic particle-in-cell algorithm on mapped computational meshes, J. Comput. Phys. **233**, 1 (2013).

[45] G. L. Delzanno, E. Camporeale, J. D. Moulton, J. E. Borovsky, E. A. MacDonald, and M. F. Thomsen, CPIC: A curvilinear particle-in-cell code for plasma-material interaction studies, IEEE T Plasma SCI **41**, 3577 (2013).

[46] L. Chacón and G. Chen, A curvilinear, fully implicit, conservative electromagnetic PIC algorithm in multiple dimensions, J. Comput. Phys. **316**, 578 (2016).

[47] S. Shahsavani, X. Chen, and G. Sanchez-Arriaga, Parametrization of current-voltage characteristics and operation domains of cylindrical emissive probes in collisionless Maxwellian plasmas at rest, Plasma Phys. Control. Fusion **63**, 115018 (2021).

[48] X. Chen and G. Sanchez-Arriaga, Kinetic features of collisionless sheaths around polarized cylindrical emitters from the orbital motion theory, Phys. Plasmas **24**, 103515 (2017).

[49] R. D. Estes and J. R. Sanmartin, Cylindrical Langmuir probes beyond the orbital-motion-limited regime, Phys. Plasmas **7**, 4320 (2000).